

# Re Doping in 2D Transition Metal Dichalcogenides as a New Route to Tailor Structural Phases and Induced Magnetism

Vidya Kochat, Amey Apte, Jordan A. Hachtel, Hiroyuki Kumazoe, Aravind Krishnamoorthy,\* Sandhya Susarla, Juan Carlos Idrobo, Fuyuki Shimojo, Priya Vashishta, Rajiv Kalia, Aiichiro Nakano, Chandra Sekhar Tiwary,\* and Pulickel M. Ajayan\*

Alloying in 2D results in the development of new, diverse, and versatile systems with prospects in bandgap engineering, catalysis, and energy storage. Tailoring structural phase transitions using alloying is a novel idea with implications in designing all 2D device architecture as the structural phases in 2D materials such as transition metal dichalcogenides are correlated with electronic phases. Here, this study develops a new growth strategy employing chemical vapor deposition to grow monolayer 2D alloys of Re-doped MoSe<sub>2</sub> with show composition tunable structural phase variations. The compositions where the phase transition is observed agree well with the theoretical predictions for these 2D systems. It is also shown that in addition to the predicted new electronic phases, these systems also provide opportunities to study novel phenomena such as magnetism which broadens the range of their applications.

2D transition metal dichalcogenide (TMD) alloys with tunable chemical composition have been gaining a lot of attention recently due to their potential in bandgap engineering, p–n junctions and valleytronics.<sup>[1–11]</sup> While most of the studies related to these phenomena were carried out on mechanically exfoliated flakes obtained from chemical vapor transport grown bulk single crystals, a few efforts have also focused on obtaining homogeneous 2D TMD alloys by chemical vapor deposition (CVD) technique.<sup>[9,12,13]</sup> Theoretical calculations and high resolution scanning transmission electron microscopy (STEM) studies reveal that doping of Group VI TMDs (MX<sub>2</sub>, where M = Mo, W, and X = S, Se) with elements from Groups V–VII energetically favors substitutional doping instead of dopants occupying interstitial and defect sites.<sup>[14,15]</sup>


Substitutional doping of Group V elements such as Nb in MoS<sub>2</sub> has been shown to result in stable p-type conduction from degenerate hole doping from Nb, whereas electron donors such as Re, Mn, etc., results in n-type doping along with spin polarized ground state according to density functional theory calculations.<sup>[15–21]</sup> Intercalation of alkali metal ions such as Li, Na, K into TMDs with a stable 2H phase (semiconducting) results in a structural modification to form a metastable metallic 1T phase, which is the result of electron transfer to the transition metal that stabilizes 1T phase having an octahedral coordination for the metal atom.<sup>[22–26]</sup> 1T-phase-stabilized TMD nanosheets have shown improved hydrogen evolution reaction (HER) performance by making the basal plane active toward HER, low resistance contacts to 2H-phase TMDs and act as excellent supercapacitor electrode materials.<sup>[22,27,28]</sup> Hence alternate routes to induce structural phase transition on a large scale can be potentially very interesting. Another subset of TMDs comprising of MoTe<sub>2</sub> and WTe<sub>2</sub> show interesting phenomena such as semimetallicity and huge linear magnetoresistance.<sup>[29–31]</sup> While WTe<sub>2</sub> is thermodynamically more stable in 1Td phase, MoTe<sub>2</sub> is more stable in 2H phase and alloy of Mo<sub>1-x</sub>W<sub>x</sub>Te<sub>2</sub> was experimentally shown to undergo

Dr. V. Kochat, A. Apte, S. Susarla, Dr. C. S. Tiwary, Prof. P. M. Ajayan  
Materials Science and Nano Engineering  
Rice University  
Houston, TX 77005, USA  
E-mail: cst.iisc@gmail.com; ajayan@rice.edu

Dr. J. A. Hachtel, Dr. J. C. Idrobo  
Center for Nanophase Materials Sciences  
Oak Ridge National Laboratory  
Oak Ridge, TN 37831, USA

H. Kumazoe, Dr. A. Krishnamoorthy, Prof. P. Vashishta, Prof. R. Kalia,  
Prof. A. Nakano  
Collaboratory for Advanced Computing and Simulations  
Department of Physics and Astronomy  
Department of Computer Science  
Department of Chemical Engineering and Materials Science  
Department of Biological Sciences  
University of Southern California  
Los Angeles, CA 90089, USA  
E-mail: kris658@usc.edu

H. Kumazoe, Prof. F. Shimojo  
Department of Physics  
Kumamoto University  
Kumamoto 860-8555, Japan

 The ORCID identification number(s) for the author(s) of this article can be found under <https://doi.org/10.1002/adma.201703754>.

DOI: 10.1002/adma.201703754

a semiconducting to semimetallic behavior as the chemical composition is varied.<sup>[32–34]</sup> Recent theoretical calculations show that the energy barrier to observe a 2H to 1T<sub>d</sub> phase transition in MoTe<sub>2</sub> is substantially lower than other TMDs and is possible to achieve by charge injection/gating and optical excitation and this barrier is further reduced in the case of Mo<sub>1–x</sub>W<sub>x</sub>Te<sub>2</sub> alloys.<sup>[35,36]</sup> On a similar note, substitutional doping at the chalcogen site was also shown to result in such a structural phase transition in the case of WSe<sub>2(1–x)</sub>Te<sub>2x</sub> for  $x > 0.7$ .<sup>[37]</sup> Most of the experimental efforts towards growing composition controlled uniform alloys to observe such a correlated electronic and structural phase transition has been through synthesis of bulk single crystals.

In this work, we have experimentally demonstrated the possibility of synthesizing 1–2 layers thin 2D solid solution/alloy from parent TMD materials, where one is stable in 2H phase and the other in 1T' phase using the CVD technique. The system we have investigated is Re-doped MoSe<sub>2</sub> where the parent components are 2H–MoSe<sub>2</sub> and 1T'–ReSe<sub>2</sub> as shown in **Figure 1a**. MoSe<sub>2</sub> has a trigonal prismatic coordination geometry and has hexagonal crystal structure with space group symmetry  $P6_3/mmc$ .<sup>[38]</sup> On the other hand, ReSe<sub>2</sub> crystallizes in distorted 1T<sub>d</sub> crystal structure with triclinic symmetry  $P\bar{1}$ .<sup>[39,40]</sup> Since each Re atom has one unpaired electron, the 1T structure undergoes Peierls distortion where Re atoms dimerize to form zig-zag Re–Re chains along *b*-axis resulting in semiconducting 1T' structure with in-plane anisotropy.<sup>[41,42]</sup> Re impurities in 2H–MoS<sub>2</sub> have been shown to be the nuclei for phase transformation to 1T domains by in situ high resolution

STEM studies.<sup>[43]</sup> Earlier studies on WS<sub>2</sub> nanotubes also demonstrated partial 2H to 1T transition under substitutional Re doping.<sup>[44]</sup> Here we have employed the CVD technique to alloy MoSe<sub>2</sub> and ReSe<sub>2</sub> during the growth phase and show that this is an excellent method of obtaining large area uniform alloys of Mo<sub>1–x</sub>Re<sub>x</sub>Se<sub>2</sub>. These alloys showed a structural phase transformation from 2H to 1T' phase as a function of Re doping. Detailed Z-contrast high-angle annular dark field (HAADF) STEM investigations were carried out to understand the atomistic mechanism of phase transformation in regions with varying Re doping. We also observed signatures of ferromagnetic ordering in these alloy systems persistent in both 2H and 1T' phases of the alloy which has been explained from spin-polarized quantum-mechanical density functional theory (DFT) calculations.

We also performed DFT calculations of relative energies of Re-doped MoSe<sub>2</sub> in the 2H and 1T' crystal structures to verify the phase transformation to the 1T' crystal structure at high Re-dopant concentrations. The DFT results, summarized in **Figure 1b**, show that the 2H polymorph of undoped MoSe<sub>2</sub> is more stable than the 1T' crystal structure by 0.35 eV per MoSe<sub>2</sub>. In contrast, the 1T' ground state of pure ReSe<sub>2</sub> is more stable than the corresponding 2H crystal structure by 0.89 eV per ReSe<sub>2</sub>. At intermediate doping concentrations, the 1T' crystal structure becomes monotonically more stable with increasing Re concentration and becomes the ground state crystal structure for Mo<sub>1–x</sub>Re<sub>x</sub>Se<sub>2</sub> systems with  $x > 0.42$ . The structural phase transformation on Re doping as predicted by our energy calculations can also be understood from the perspective of crystal

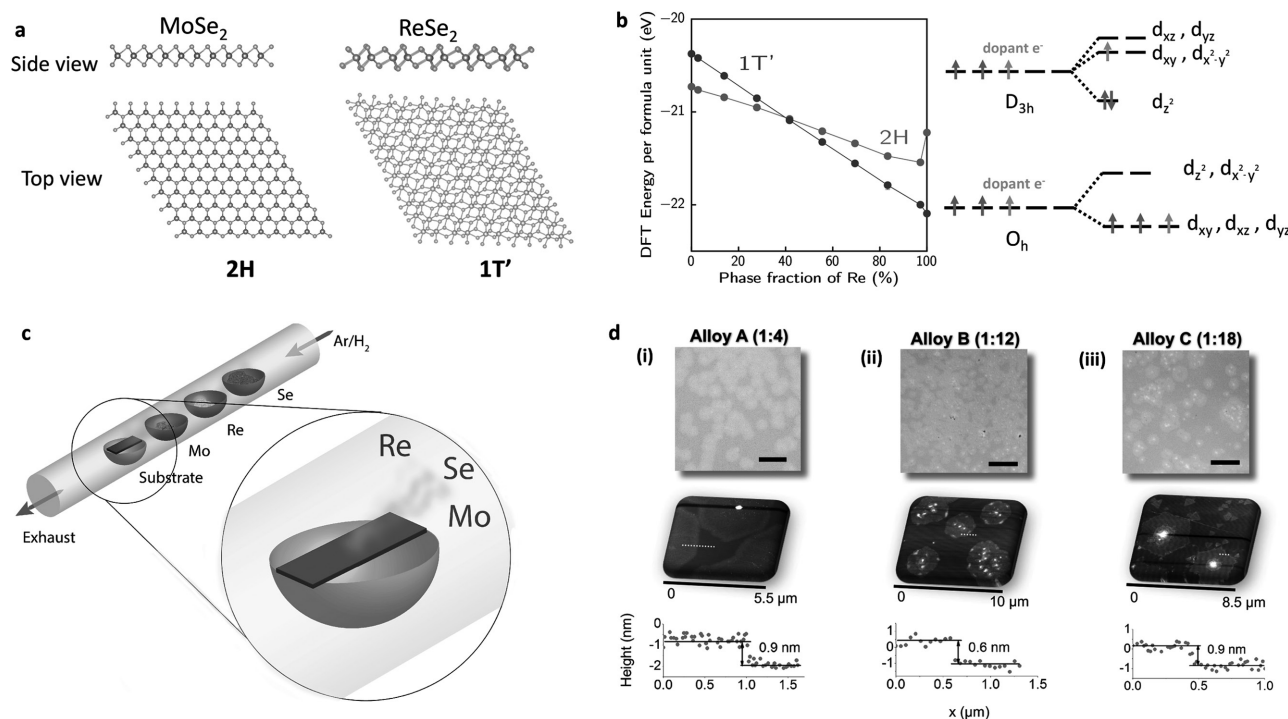


**Figure 1.** a) The lowest energy crystal structure of MoSe<sub>2</sub> and ReSe<sub>2</sub>. b) Energy of the 2H and 1T' phases of MoSe<sub>2</sub> with increase in Re doping fraction. The splitting of the degenerate 4d orbitals of Mo is shown for 2H (D<sub>3h</sub>) and 1T' (distorted O<sub>h</sub>) phases with filling of extra electron from Re dopant. c) Schematic of the CVD growth setup illustrating simultaneous sublimation of Mo, Re, and Se precursors. d) Optical and AFM images of the Mo<sub>1–x</sub>Re<sub>x</sub>Se<sub>2</sub> alloys grown using the CVD technique.

field theory and is analogous to the structural transformation induced by lithiation treatment.<sup>[45–47]</sup> The arrangement of the negative chalcogen ions in the local environment of transition metal ions (Mo) lifts the degeneracy of the Mo 4d orbitals. In the 2H phase, where Mo has a trigonal prismatic coordination with Se ions, the 4d orbitals split to form three energy levels: (1)  $d_{z^2}$  which is lowest in energy, (2) degenerate  $d_{xy}$  and  $d_{x^2-y^2}$ , and (3) degenerate  $d_{xz}$  and  $d_{yz}$ . The octahedral coordination of Mo in 1T phase in turn splits the degenerate 4d Mo orbitals into two energy levels: (1) degenerate  $d_{xy}$ ,  $d_{yz}$ ,  $d_{xz}$  having lowest energy and (2)  $d_{z^2}$  and  $d_{x^2-y^2}$ , which are the higher energy states as shown in Figure 1b. Re doping into  $\text{MoSe}_2$  lattice leads to substitution of Re in Mo sites, with the addition of an extra electron into lattice. This extra electron is promoted to the higher energy level in trigonal prismatic coordination geometry where the incomplete filling now destabilizes the 2H phase, whereas in the octahedral coordination geometry this extra electron fills the lower energy state increasing the stability of 1T phase. This shows that reorganization of the Mo 4d orbitals on electron doping by Re results in structural transformation from 2H to a stable 1T phase.

The CVD setup for growth of  $\text{Mo}_{1-x}\text{Re}_x\text{Se}_2$  alloys is shown in schematic Figure 1c. For composition controlled growth of the alloys, the Mo and Re precursors were taken in fixed weight

ratios (1:4 for Alloy A, 1:12 for Alloy B, and 1:18 for Alloy C). The optical micrographs and AFM images of the flakes grown using this technique is shown in Figure 1d. The morphology of the flakes and their thickness were investigated in detail using AFM, which showed sub-nm average thickness indicating that these flakes are mostly monolayers. The compositional and structural characterization was carried out using Raman spectroscopy, X-ray photoelectron spectroscopy (XPS) and STEM. Raman spectra collected from these samples display marked changes for alloys with increasing Re precursor concentration in comparison to the spectra obtained for CVD grown pure  $\text{MoSe}_2$  and  $\text{ReSe}_2$  as shown in Figure 2a. The intensity of the  $\text{MoSe}_2$   $A_{1g}$  peak at  $238\text{ cm}^{-1}$  is reduced on alloying with Re in alloy A and B along with the appearance of additional peaks at 122, 152, 220, and  $250\text{ cm}^{-1}$ . The decrease in the intensity of  $A_{1g}$  mode which results from the out-of-plane vibration of Se atoms, can be attributed to the softening or renormalization of  $A_{1g}$  phonon due to significant changes in the electron–phonon coupling arising from the n-type doping from Re.<sup>[48]</sup> We also observe splitting of the  $E_{2g}$  mode (about  $288\text{ cm}^{-1}$ ) which is a combination of LO and TO phonons due to the polar nature of  $\text{MoSe}_2$  crystal.<sup>[49,50]</sup> In earlier studies on  $\text{MoSe}_2$  samples with Se vacancies, additional peaks around 150 and  $250\text{ cm}^{-1}$  were reported from the momentum contribution from phonons with

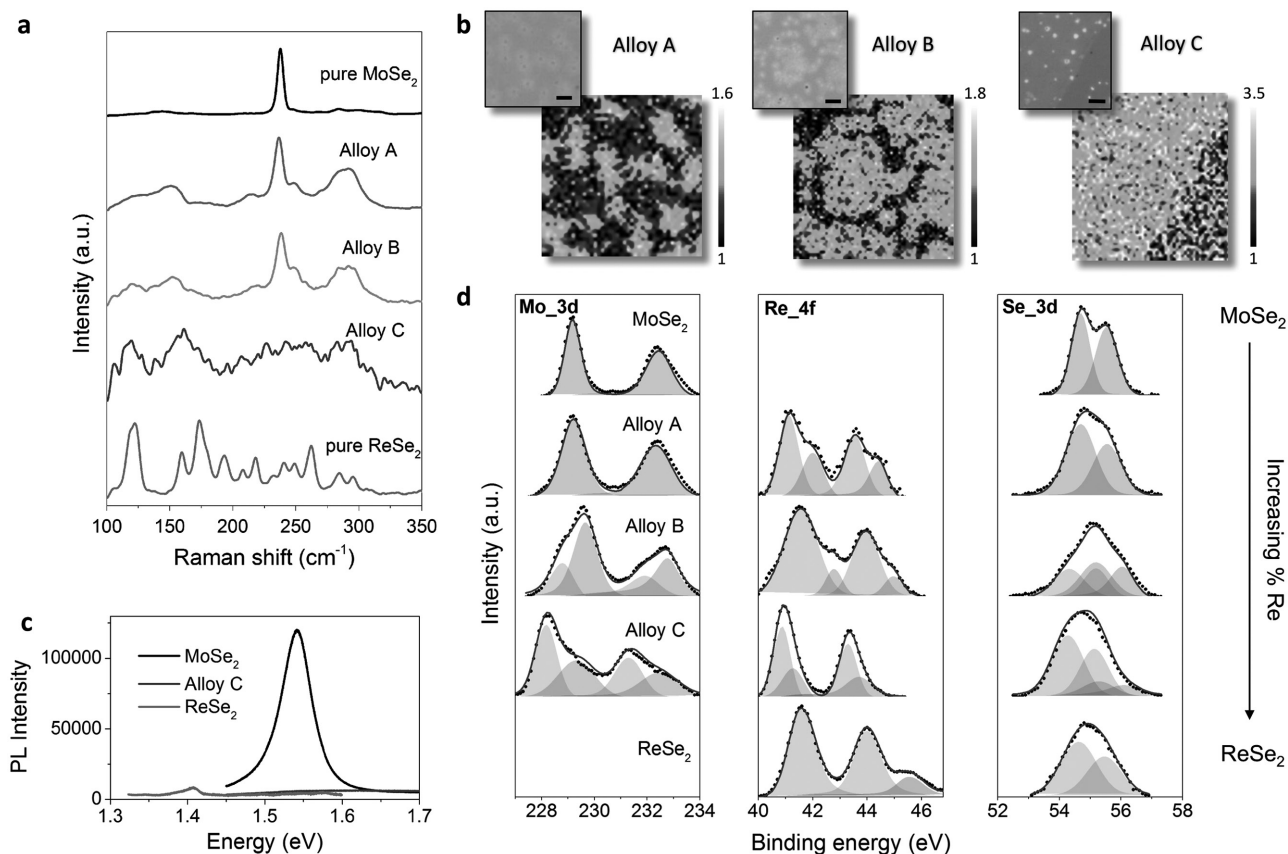


**Figure 2.** a) Raman spectra of pristine CVD grown  $\text{MoSe}_2$  and  $\text{ReSe}_2$  along with the alloys. b) Ratio map of Raman intensity of  $A_{1g}/E_{2g}$  for Alloys A and B and  $E_{1g}^1/A_{1g}$  for Alloy C. c) Photoluminescence characterization for  $\text{MoSe}_2$ , alloys, and  $\text{ReSe}_2$ . The alloys showed completely quenched PL. d) XPS characterization of Mo 3d, Re 4f, and Se 3d orbitals showing evolution from 2H to 1T phase on increasing Re %. The blue curve represents the XPS fits ( $R^2 \approx 0.9$ ) to the data represented by black circles.

large wave vectors activated by defects.<sup>[51,52]</sup> Raman spectrum of 1T-phase MoSe<sub>2</sub> also shows peaks 106, 151, and 221 cm<sup>-1</sup> which could also be observed in alloy B.<sup>[53]</sup> ReSe<sub>2</sub> has 18 Raman-active A<sub>g</sub> modes in the range 100–300 cm<sup>-1</sup> arising from lower structural symmetry and nondegenerate normal modes arising due to atomic displacement from inversion center as shown.<sup>[42]</sup> The Raman maps in Figure 2b shows intensity ratio (A<sub>1g</sub>/E<sub>12g</sub> for Alloys A and B, while reverse for Alloy C) showing the uniform nature of the A<sub>1g</sub> peak reduction all over the flakes. The photoluminescence (PL) measurements in Figure 2c reveal strong PL peak for MoSe<sub>2</sub> and ReSe<sub>2</sub> at 1.54 and 1.4 eV, respectively, whereas the PL was completely quenched for Alloy C. Further insight into the composition and bonding state information was obtained from XPS investigations shown in Figure 2d. The spin-orbit split 3d<sub>5/2</sub> and 3d<sub>3/2</sub> orbitals of Mo displayed peaks at binding energies of 229.1 and 232.3 eV, respectively, consistent with 2H-phase MoSe<sub>2</sub> with oxidation state of +4. For alloy A, we did not observe much shift/splitting for the Mo 3d peaks and the Se 3d peak could also be fit using a two-peak fitting for the 3d<sub>5/2</sub> and 3d<sub>3/2</sub> orbitals, but at the same time spin-orbit split Re 4f<sub>7/2</sub> and 4f<sub>5/2</sub> peaks showed additional splitting due to an interplay between 2H and 1T coordination. With increase in Re concentration, the Mo 3d peaks showed peak shifts toward lower binding energy values which can be corroborated with split peaks and the Se 3d peak became a convolution of four peaks clearly demonstrating the change in coordination of Mo from trigonal prismatic to octahedral geometry.<sup>[24]</sup> For Re 4f<sub>5/2</sub> and 4f<sub>7/2</sub> states, we find an oxidation state of +4 and the larger intensity for the lower energy split peaks indicating tendency toward octahedral coordination. The blue colored peak in ReSe<sub>2</sub> at ≈46 eV corresponds to the 4f<sub>7/2</sub> orbital of Re in NH<sub>4</sub>ReO<sub>4</sub> (unreacted reactant).

The effect of the Re doping on the structure can be more clearly seen in **Figure 3**, which contains a series of STEM images of different regions of the Re-doped MoSe<sub>2</sub> sample, showing different structural configurations. Figure 3a shows an HAADF image of a large monolayer area in the 2H phase. In HAADF imaging the contrast of an atom (or column of atoms) is directly tied to the atomic number (or Z value of the column), hence a heavy atom like Re (Z = 73) stands out compared to the lighter atoms such as Mo (Z = 42) and Se (Z = 36). Figure 3b shows the HAADF intensity histograms of the metal sites (i) and chalcogenide sites (ii) for the image shown in Figure 3a. From the metal site histogram, the difference between the Mo and Re intensities can be clearly distinguished. The atoms are then identified and labeled as more likely to be Mo or more likely to be Re based off of their HAADF intensities and sites. From the labeled image, the Re doping concentration in the region can be quantified, which is determined to be ≈23%. This corresponds well with the calculations in Figure 1 which shows that below 40% Re doping the 2H phase should be the preferred state. Figure 3c shows the location of the Mo, Re, and Se atoms throughout the sample, showing that in this region the Re dopants are uniformly dispersed throughout the MoSe<sub>2</sub> lattice. However, Figure 3d shows that the structure changes within the same sample in different locations. Here, a phase transition between the 2H and 1T' phases is observed over a small, sub-nm distance. This shows that these systems exist as solid solutions with homogeneous structural phases. In both

the 2H and 1T' phases the high Z-value of Re makes it easy to identify, which is shown in Figure 3e (2H phase in (i) and (ii), and 1T' phase in (iii) and (iv)). Quantification of the Re concentration akin to that performed in Figure 3a–c is difficult in the 1T' phase due to significant structural variations over large areas and a higher sensitivity to the electron beam, and is not performed. Instead, a pure ReSe<sub>2</sub> sample is imaged and shown in Figure 3f as a reference of a highly regular 1T' crystal structure. Here it shows that the Re atoms group into 2 × 2 unit cells with an orthorhombic periodicity. Figure 3g shows a high-magnification view of the Re-doped MoSe<sub>2</sub> structure in the 1T' phase, the same 2 × 2 unit cells are observed but many with only two or three bright atoms. The stark contrast between Re and Mo allows us to straightforwardly label the atoms in these positions as Mo based off of their Z-contrast to demonstrate the presence of Mo atoms in the 1T' crystal structure, which are also uniformly distributed throughout the 1T' region. Additionally, it is clear that in this region, the Re atoms outnumber the Mo atoms indicating that the doping concentration is above the 40% threshold where the 2H phase ceases to be the preferred structure.

The doping of Re in MoSe<sub>2</sub> lattice can have other interesting phenomena apart from the structural phase transition due to extra electron added to the Mo<sub>1-x</sub>Re<sub>x</sub>Se<sub>2</sub> alloy system per Re atom which can manifest in a magnetic ground state as suggested by DFT calculations.<sup>[14,21]</sup> In order to investigate the possibility of magnetism in the Mo<sub>1-x</sub>Re<sub>x</sub>Se<sub>2</sub> alloy samples, magnetic measurements were performed using a Quantum Design SQUID magnetometer from 300 K down to 10 K. The total magnetic moment of the samples, Alloy A which shows 2H phase and Alloy C which shows 1T' phase measured as a function of the applied field at 300 and 10 K are shown in **Figure 4a**. At 300 K, we observe a large diamagnetic signal along with a superimposed weak hysteresis curve near zero field, suggesting possibility of ferromagnetic ordering even at room temperature. On cooling down to 10 K, we observe the field dependence to be that of ferromagnetism superimposed on paramagnetism. Figure 4a(iii) shows the low field dependence of measured moment at 10 K for both the alloy samples clearly showing hysteresis with coercive field values of 170 and 70 Oe for alloy A and C, respectively indicating higher coercivity for alloys in 2H phase. The zero-field cooled (ZFC) and field cooled (FC) measurements as a function of temperature with H = 100 Oe is shown in Figure 4b. The splitting between the ZFC and FC curves from 300 K suggest ferromagnetic behavior persists to above room temperatures in these alloys. The sharp upturn in FC-ZFC in the low-temperature regime (T < 20 K) is indicative of the superimposed paramagnetic behavior of Re-doped MoSe<sub>2</sub> samples which can arise from the uncorrelated spins in these systems. The divergence between the FC and ZFC curves and the appearance of a peak (or cusp) in the temperature regime (20 K < T < 80 K) are signatures of frustrated magnetic systems such as spin glasses.<sup>[54–56]</sup> The negative Curie–Weiss temperature values obtained from fitting the high-temperature m-T data indicates the presence of antiferromagnetic correlations competing with ferromagnetic order. This sharp upturn resulting in the anomalous peak is more prominent in the case of alloys in 1T' phase. These measurements reveal the presence of competing magnetic correlations in these alloys.



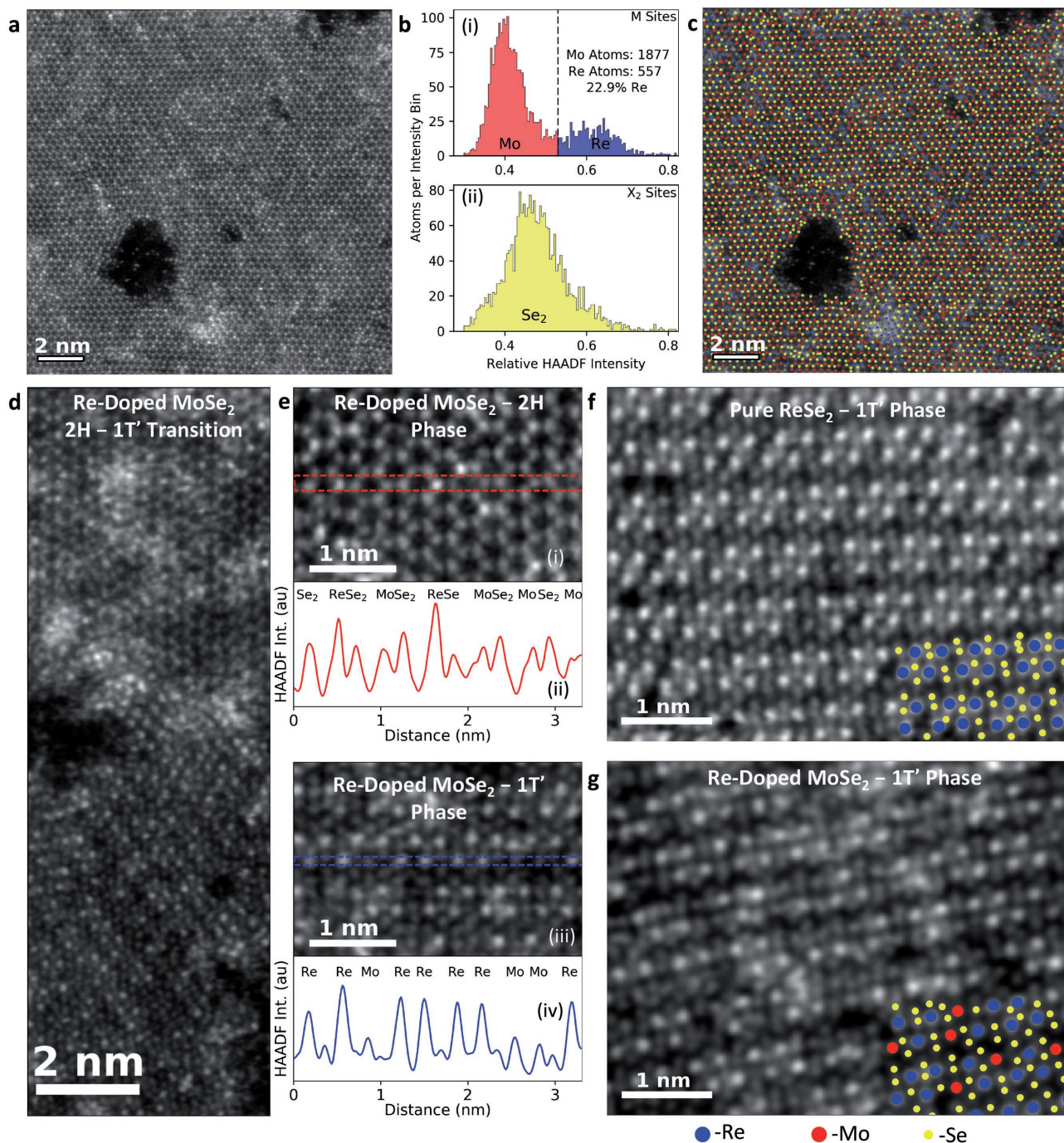


**Figure 3.** a) High-angle annular dark field image of Re-doped  $\text{MoSe}_2$  monolayer in 2H phase. b) Histogram of HAADF intensities for (i) metal sites and (ii) chalcogenide sites showing that Re doping in 2H region  $<40\%$ . c) Atom-labeled image of (a) showing Re dopants uniformly spaced throughout  $\text{MoSe}_2$  lattice. d) HAADF image showing phase transition from 2H to  $1\text{T}'$ . e) Line profiles of HAADF intensities showing how strong difference in Z-contrast between Mo (42) and Re (73) allows for easy distinction between atoms in both 2H (i and ii), and  $1\text{T}'$  (iii and iv) phases. f) HAADF image of pure  $\text{ReSe}_2$  in  $1\text{T}'$  phase as reference. g) High-magnification view of Re-doped  $\text{MoSe}_2$  monolayer in  $1\text{T}'$  phase. Atoms in bottom left corner are labeled to show presence of Mo atoms in  $1\text{T}'$  region.

In order to understand the electronic origin of the unique magnetism in 2D  $\text{Mo}_{1-x}\text{Re}_x\text{Se}_2$ , we performed quantum molecular dynamics simulations, which follow the trajectories of all atoms while computing interatomic forces quantum mechanically from first principles (see the Experimental

Section for simulation details). We simulated both 2H phase ( $x = 0.14$ ) and  $1\text{T}'$  phase ( $x = 0.83$ ). Figure 4c,d, shows partial spin densities-of-states (DOS) for 2H and  $1\text{T}'$  phases, respectively, in the absence of magnetic field at temperature 0 K. Slight asymmetry between spin-up and spin-down DOSs

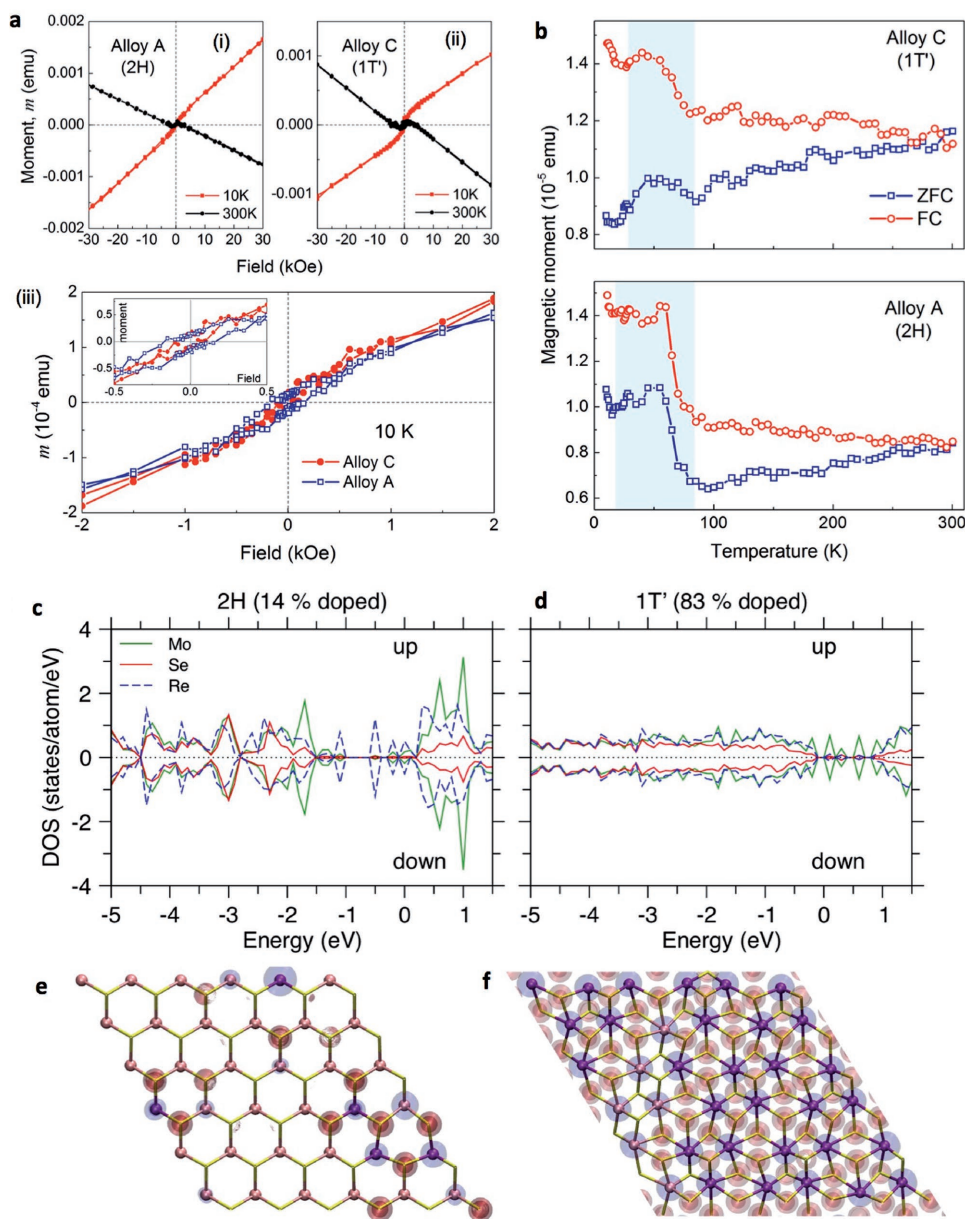


**Figure 4.** a) Magnetic measurements of moment as a function of applied field for samples Alloy A (i) and Alloy C (ii) at  $T = 10$  and  $300$  K. (iii) The low field behavior for the alloys display hysteresis at  $10$  K. The inset shows the zoomed in region near zero field. b) The temperature dependence of total moment obtained by ZFC and FC and measured in a field of  $100$  Oe is shown for Alloy A and C. c, d) Partial spin densities-of-states for  $2H$  ( $x = 0.14$ ) and  $1T'$  ( $x = 0.83$ ) phases. Solid green and red lines are for Mo and Se, respectively, whereas blue dashed line is for Re. The origin of the energy is the Fermi energy. e, f) Up (blue) and down (red) spin densities of  $2H$  ( $x = 0.14$ ) and  $1T'$  ( $x = 0.83$ ) phases. In (e), isosurfaces of  $7 \times 10^{-4}$  a.u. $^{-3}$  (blue) and  $-1.5 \times 10^{-4}$  a.u. $^{-3}$  (red) are shown, while in (f), those of  $1.5 \times 10^{-4}$  a.u. $^{-3}$  (blue), and  $-1 \times 10^{-4}$  a.u. $^{-3}$  (red) are shown. Pink, purple, and yellow spheres represent Mo, Re, and Se atoms, respectively.

amounts to small total magnetization of  $2.779 \times 10^{-3} \mu_B$  and  $6.092 \times 10^{-4} \mu_B$  per chemical unit ( $Mo_{1-x}Re_xSe_2$ ) in the  $2H$  and  $1T'$  phases, respectively. Figure 4e, f, shows spin densities for the  $2H$  and  $1T'$  configurations. We found that Re atoms (colored purple in Figure 4) tend to cluster, which produce Re–Se–Re groups even at low Re concentration ( $x = 0.14$ , Figure 4e). Figure 4c shows clear ferromagnetic ordering of these next nearest-neighbor Re pairs, shown by positive (colored

blue) spin densities around Re atoms. In contrast, Mo atoms have no spin. A similar pattern is also observed at the high Re concentration ( $x = 0.83$ , Figure 4f). Figure S1 (Supporting Information) shows the corresponding magnetic properties at a temperature of  $600$  K. The high temperature suppresses the magnetism, though major trends remain unchanged.

In summary, we have demonstrated alloying of 2D materials of structurally different phases and show that the structure of



the alloy is tunable by the concentration of the parent phases. The Re doping strategy can be generalized to the system of  $\text{MX}_2$  ( $M = \text{Mo}, \text{W}$ , and  $X = \text{S}, \text{Se}$ ) TMDs to alter the stacking sequences by electron donation. We find interesting new phenomena arising in these 2D systems such as magnetic ordering which can have useful applications in the field of spintronics.

## Experimental Section

**Growth of  $\text{Mo}_{1-x}\text{Re}_x\text{Se}_2$  alloys:**  $\text{Mo}_{1-x}\text{Re}_x\text{Se}_2$  2D alloy samples were grown via chemical vapor deposition. In a 2 in. quartz tube, ammonium molybdate, and ammonium perchlorate powders in fixed weight ratios were taken in separate porcelain boats (as described in Figure 1c and the main text). Sapphire substrates were cleaned with acetone/isopropanol and placed downstream of ammonium molybdate and selenium powder was kept upstream of ammonium perchlorate, respectively. The tube was filled with 15%  $\text{H}_2$  in Ar gas and the temperature was ramped to 600 °C and held for 15–20 min before cooling down ambiently.

Characterization of alloys: Raman and photoluminescence spectra was recorded on a Renishaw inVia confocal microscope equipped with a 532 nm laser focused via 50X objective lens and 10s acquisition times. Atomic force micrographs were obtained on a Bruker Multimode 8 AFM with NanoScope V controller operating in tapping mode. XPS spectra were recorded using a PHI Quantera II automated scanning XPS module with Al  $K\alpha$  X-ray source (1486.6 eV, 50 W) and pass energy of 26 eV. Magnetic measurements were carried out using an MPMS SQUID system from Quantum Design from 300 to 10 K. STEM Analysis: STEM imaging performed on a Nion aberration-corrected UltraSTEM 100 operated at 60 kV accelerating voltage.<sup>[57]</sup> Quantitative analysis of Re concentration in the 2H phase was accomplished using an in-house script written in Python. The function “peak\_local\_max” within the SciKit Imaging python module was utilized in the algorithm implemented to identify the atomic positions and their respective intensities.<sup>[58]</sup> The metal sites and chalcogenide sites are distinguished from the orientation of the three nearest neighbors of each atom and then the final HAADF intensity histogram for each site. Threshold between Mo and Re is set by fitting Gaussians to the Re and Mo peaks and placing the threshold at the overlap point.

## Supporting Information

Supporting Information is available from the Wiley Online Library or from the author.

## Acknowledgements

V.K. and A.A. contributed equally to this work. This work was supported by the Computational Materials Sciences Program funded by the U.S. Department of Energy, Office of Science, Basic Energy Sciences, under Award No. DE-SC00014607. The simulations were performed at the Argonne Leadership Computing Facility under the DOE INCITE program and at the Center for High Performance Computing of the University of Southern California. Microscopy research performed as part of a user proposal at Oak Ridge National Laboratory's Center for Nanophase Materials Sciences (CNMS), which is a U.S. Department of Energy, Office of Science User Facility (J.A.H. and J.C.I.).

## Conflict of Interest

The authors declare no conflict of interest.

## Keywords

2D materials, alloys, DFT calculations, magnetic properties, phase transition

Received: July 5, 2017

Revised: August 21, 2017

Published online: October 9, 2017

- [1] S.-H. Su, Y.-T. Hsu, Y.-H. Chang, M.-H. Chiu, C.-L. Hsu, W.-T. Hsu, W.-H. Chang, J.-H. He, L.-J. Li, *Small* **2014**, *10*, 2589.
- [2] J.-G. Song, G. H. Ryu, S. J. Lee, S. Sim, C. W. Lee, T. Choi, H. Jung, Y. Kim, Z. Lee, J.-M. Myoung, C. Dussarrat, C. Lansalot-Matras, J. Park, H. Choi, H. Kim, *Nat. Commun.* **2015**, *6*, 7817.
- [3] Q. Feng, Y. Zhu, J. Hong, M. Zhang, W. Duan, N. Mao, J. Wu, H. Xu, F. Dong, F. Lin, C. Jin, C. Wang, J. Zhang, L. Xie, *Adv. Mater.* **2014**, *26*, 2648.
- [4] S. Yoshida, Y. Kobayashi, R. Sakurada, S. Mori, Y. Miyata, H. Mogi, T. Koyama, O. Takeuchi, H. Shigekawa, *Sci. Rep.* **2015**, *5*, 14808.
- [5] A. Kutana, E. S. Penev, B. I. Yakobson, *Nanoscale* **2014**, *6*, 5820.
- [6] M. Zhang, J. Wu, Y. Zhu, D. O. Dumcenco, J. Hong, N. Mao, S. Deng, Y. Chen, Y. Yang, C. Jin, S. H. Chaki, Y.-S. Huang, J. Zhang, L. Xie, *ACS Nano* **2014**, *8*, 7130.
- [7] Y. Chen, D. O. Dumcenco, Y. Zhu, X. Zhang, N. Mao, Q. Feng, M. Zhang, J. Zhang, P.-H. Tan, Y.-S. Huang, L. Xie, *Nanoscale* **2014**, *6*, 2833.
- [8] Y. Chen, J. Xi, D. O. Dumcenco, Z. Liu, K. Suenaga, D. Wang, Z. Shuai, Y.-S. Huang, L. Xie, *ACS Nano* **2013**, *7*, 4610.
- [9] Y. Gong, Z. Liu, A. R. Lupini, G. Shi, J. Lin, S. Najmaei, Z. Lin, A. L. Elías, A. Berkdemir, G. You, H. Terrones, M. Terrones, R. Vajtai, S. T. Pantelides, S. J. Pennycook, J. Lou, W. Zhou, P. M. Ajayan, *Nano Lett.* **2014**, *14*, 442.
- [10] G. Wang, C. Robert, A. Suslu, B. Chen, S. Yang, S. Alamdari, I. C. Gerber, T. Amand, X. Marie, S. Tongay, B. Urbaszek, *Nat. Commun.* **2015**, *6*, 10110.
- [11] J. Xi, T. Zhao, D. Wang, Z. Shuai, *J. Phys. Chem. Lett.* **2014**, *5*, 285.
- [12] L. Yang, Q. Fu, W. Wang, J. Huang, J. Zhang, B. Xiang, *Nanoscale* **2015**, *7*, 10490.
- [13] H. Li, X. Duan, X. Wu, X. Zhuang, H. Zhou, Q. Zhang, X. Zhu, W. Hu, P. Ren, P. Guo, L. Ma, X. Fan, X. Wang, J. Xu, A. Pan, X. Duan, *J. Am. Chem. Soc.* **2014**, *136*, 3756.
- [14] K. Dolui, I. Rungger, C. Das Pemmaraju, S. Sanvito, *Phys. Rev. B* **2013**, *88*, 75420.
- [15] Y. Lin, D. O. Dumcenco, H.-P. Komsa, Y. Niimi, A. V. Krashenninnikov, Y.-S. Huang, K. Suenaga, *Adv. Mater.* **2014**, *26*, 2857.
- [16] J. Suh, T.-E. Park, D.-Y. Lin, D. Fu, J. Park, H. J. Jung, Y. Chen, C. Ko, C. Jang, Y. Sun, R. Sinclair, J. Chang, S. Tongay, J. Wu, *Nano Lett.* **2014**, *14*, 6976.
- [17] M. R. Laskar, D. N. Nath, L. Ma, E. W. Lee, C. H. Lee, T. Kent, Z. Yang, R. Mishra, M. A. Roldan, J.-C. Idrobo, S. T. Pantelides, S. J. Pennycook, R. C. Myers, Y. Wu, S. Rajan, *Appl. Phys. Lett.* **2014**, *104*, 92104.
- [18] S. Das, M. Demarteau, A. Roelofs, *Appl. Phys. Lett.* **2015**, *106*, 173506.
- [19] K. Zhang, S. Feng, J. Wang, A. Azcatl, N. Lu, R. Addou, N. Wang, C. Zhou, J. Lerach, V. Bojan, M. J. Kim, L.-Q. Chen, R. M. Wallace, M. Terrones, J. Zhu, J. A. Robinson, *Nano Lett.* **2015**, *15*, 6586.
- [20] S. Mula, Y.-S. Huang, C.-H. Ho, Y.-C. Lin, K. Suenaga, *Jpn. J. Appl. Phys.* **2015**, *54*, 04DH05.
- [21] P. Zhao, J. Zheng, P. Guo, Z. Jiang, L. Cao, Y. Wan, *Comput. Mater. Sci.* **2017**, *128*, 287.
- [22] D. Voiry, M. Salehi, R. Silva, T. Fujita, M. Chen, T. Asefa, V. B. Shenoy, G. Eda, M. Chhowalla, *Nano Lett.* **2013**, *13*, 6222.

- [23] R. Koppera, D. Voiry, S. E. Yalcin, B. Branch, G. Gupta, A. D. Mohite, M. Chhowalla, *Nat. Mater.* **2014**, *13*, 1128.
- [24] D. Voiry, A. Goswami, R. Koppera, C. d. C. e. Silva, D. Kaplan, T. Fujita, M. Chen, T. Asefa, M. Chhowalla, *Nat. Chem.* **2015**, *7*, 45.
- [25] H. Fang, M. Tosun, G. Seol, T. C. Chang, K. Takei, J. Guo, A. Javey, *Nano Lett.* **2013**, *13*, 1991.
- [26] R. Zhang, I.-L. Tsai, J. Chapman, E. Khestanova, J. Waters, I. V. Grigorieva, *Nano Lett.* **2016**, *16*, 629.
- [27] D. Voiry, J. Yang, M. Chhowalla, *Adv. Mater.* **2016**, *28*, 6197.
- [28] M. Acerce, D. Voiry, M. Chhowalla, *Nat. Nano* **2015**, *10*, 313.
- [29] D. H. Keum, S. Cho, J. H. Kim, D.-H. Choe, H.-J. Sung, M. Kan, H. Kang, J.-Y. Hwang, S. W. Kim, H. Yang, K. J. Chang, Y. H. Lee, *Nat. Phys.* **2015**, *11*, 482.
- [30] Y. Qi, P. G. Naumov, M. N. Ali, C. R. Rajamathi, W. Schnelle, O. Barkalov, M. Hanfland, S.-C. Wu, C. Shekhar, Y. Sun, V. Süß, M. Schmidt, U. Schwarz, E. Pippel, P. Werner, R. Hillebrand, T. Förster, E. Kampert, S. Parkin, R. J. Cava, C. Felser, B. Yan, S. A. Medvedev, *Nat. Commun.* **2016**, *7*, 11038.
- [31] M. N. Ali, J. Xiong, S. Flynn, J. Tao, Q. D. Gibson, L. M. Schoop, T. Liang, N. Haldolaarachchige, M. Hirschberger, N. P. Ong, R. J. Cava, *Nature* **2014**, *514*, 205.
- [32] T. A. Empante, Y. Zhou, V. Klee, A. E. Nguyen, I.-H. Lu, M. D. Valentin, S. A. Naghibi Alvililar, E. Preciado, A. J. Berges, C. S. Merida, M. Gomez, S. Bobek, M. Isarraraz, E. J. Reed, L. Bartels, *ACS Nano* **2017**, *11*, 900.
- [33] C. H. Naylor, W. M. Parkin, Z. Gao, H. Kang, M. Noyan, R. B. Wexler, L. Z. Tan, Y. Kim, C. E. Kehayias, F. Streller, Y. R. Zhou, R. Carpick, Z. Luo, Y. W. Park, A. M. Rappe, M. Drndić, J. M. Kikkawa, A. T. C. Johnson, *2D Mater.* **2017**, *4*, 21008.
- [34] D. Rhodes, D. A. Chenet, B. E. Janicek, C. Nyby, Y. Lin, W. Jin, D. Edelberg, E. Mannebach, N. Finney, A. Antony, T. Schiros, T. Klarr, A. Mazzoni, M. Chin, Y. C. Chiu, W. Zheng, Q. R. Zhang, F. Ernst, J. I. Dadap, X. Tong, J. Ma, R. Lou, S. Wang, T. Qian, H. Ding, R. M. Osgood, D. W. Paley, A. M. Lindenberg, P. Y. Huang, A. N. Pasupathy, M. Dubey, J. Hone, L. Balicas, *Nano Lett.* **2017**, *17*, 1616.
- [35] C. Zhang, S. KC, Y. Nie, C. Liang, W. G. Vandenberghe, R. C. Longo, Y. Zheng, F. Kong, S. Hong, R. M. Wallace, K. Cho, *ACS Nano* **2016**, *10*, 7370.
- [36] Y. Li, K.-A. N. Duerloo, K. Wauson, E. J. Reed, *Nat. Commun.* **2016**, *7*, 10671.
- [37] P. Yu, J. Lin, L. Sun, Q. L. Le, X. Yu, G. Gao, C.-H. Hsu, D. Wu, T.-R. Chang, Q. Zeng, F. Liu, Q. J. Wang, H.-T. Jeng, H. Lin, A. Trampert, Z. Shen, K. Suenaga, Z. Liu, *Adv. Mater.* **2017**, *29*, 1603991.
- [38] X. Wang, Y. Gong, G. Shi, W. L. Chow, K. Keyshar, G. Ye, R. Vajtai, J. Lou, Z. Liu, E. Ringe, B. K. Tay, P. M. Ajayan, *ACS Nano* **2014**, *8*, 5125.
- [39] M. Hafeez, L. Gan, H. Li, Y. Ma, T. Zhai, *Adv. Mater.* **2016**, *28*, 8296.
- [40] H. H. Murray, S. P. Kelty, R. R. Chianelli, C. S. Day, *Inorg. Chem.* **1994**, *33*, 4418.
- [41] B. Jariwala, D. Voiry, A. Jindal, B. A. Chalke, R. Bapat, A. Thamizhavel, M. Chhowalla, M. Deshmukh, A. Bhattacharya, *Chem. Mater.* **2016**, *28*, 3352.
- [42] D. Wolverson, S. Crampin, A. S. Kazemi, A. Ilie, S. J. Bending, *ACS Nano* **2014**, *8*, 11154.
- [43] Y.-C. Lin, D. O. Dumcenco, Y.-S. Huang, K. Suenaga, *Nat. Nanotechnol.* **2013**, *9*, 391.
- [44] A. N. Enyashin, L. Yadgarov, L. Houben, I. Popov, M. Weidenbach, R. Tenne, M. Bar-Sadan, G. Seifert, *J. Phys. Chem. C* **2011**, *115*, 24586.
- [45] D. Voiry, A. Mohite, M. Chhowalla, *Chem. Soc. Rev.* **2015**, *44*, 2702.
- [46] X. Sun, Z. Wang, Z. Li, Y. Q. Fu, *Sci. Rep.* **2016**, *6*, 26666.
- [47] M. Kan, J. Y. Wang, X. W. Li, S. H. Zhang, Y. W. Li, Y. Kawazoe, Q. Sun, P. Jena, *J. Phys. Chem. C* **2014**, *118*, 1515.
- [48] B. Chakraborty, A. Bera, D. V. S. Muthu, S. Bhowmick, U. V. Waghmare, A. K. Sood, *Phys. Rev. B: Condens. Matter Mater. Phys.* **2012**, *85*, 1.
- [49] A. Molina-Sánchez, L. Wirtz, *Phys. Rev. B: Condens. Matter Mater. Phys.* **2011**, *84*, 155413.
- [50] D. Nam, J.-U. Lee, H. Cheong, *Sci. Rep.* **2015**, *5*, 17113.
- [51] M. Mahjouri-Samani, L. Liang, A. Oyedele, Y.-S. Kim, M. Tian, N. Cross, K. Wang, M.-W. Lin, A. Boulesbaa, C. M. Rouleau, A. A. Puretzky, K. Xiao, M. Yoon, G. Eres, G. Duscher, B. G. Sumpter, D. B. Geohegan, *Nano Lett.* **2016**, *16*, 5213.
- [52] P. Soubelet, A. E. Bruchhausen, A. Fainstein, K. Nogajewski, C. Faugeras, *Phys. Rev. B* **2016**, *93*, 155407.
- [53] U. Gupta, B. S. Naidu, U. Maitra, A. Singh, S. N. Shirodkar, U. V. Waghmare, C. N. R. Rao, *APL Mater.* **2014**, *2*, 92802.
- [54] H. S. S. R. Matte, K. S. Subrahmanyam, C. N. R. Rao, *J. Phys. Chem. C* **2009**, *113*, 9982.
- [55] C. N. R. Rao, H. S. S. R. Matte, K. S. Subrahmanyam, U. Maitra, *Chem. Sci.* **2012**, *3*, 45.
- [56] W. R. Chen, F. C. Zhang, J. Miao, B. Xu, X. L. Dong, L. X. Cao, X. G. Qiu, B. R. Zhao, P. Dai, *Appl. Phys. Lett.* **2005**, *87*, 42508.
- [57] O. L. Krivanek, G. J. Corbin, N. Dellby, B. F. Elston, R. J. Keyse, M. F. Murfitt, C. S. Own, Z. S. Szilagyi, J. W. Woodruff, *Ultramicroscopy* **2008**, *108*, 179.
- [58] S. van der Walt, J. L. Schönberger, J. Nunez-Iglesias, F. Boulogne, J. D. Warner, N. Yager, E. Gouillart, T. Yu, *PeerJ* **2014**, *2*, e453.